LANGMUIR Article
Cite This: Langmuir 2019, 35, 12460−12468
pubs.acs.org/Langmuir

pH-Controlled Chiral Packing and Self-Assembly of a Coumarin Tetrapeptide

McKensie L. Mason,[†] Remy F. Lalisse,[†] Tyler J. Finnegan,[†] Christopher M. Hadad,[†] David A. Modarelli,[‡] and Jon R. Parquette*[,†]

[†]Department of Chemistry and Biochemistry, The Ohio State University, 100 W. 18th Avenue, Columbus, Ohio 43210, United States

[‡]Department of Chemistry and The Center for Laser and Optical Spectroscopy, Knight Chemical Laboratory, The University of Akron, Akron, Ohio 44325-3601, United States

Supporting Information

A coumarin−tetrapeptide conjugate, EFEK(DAC)−NH_2 (**1**), is reported to undergo a pH-dependent interconversion between nanotubes and nanoribbons. An examination of zeta potential measurements, circular dichroism (CD) spectra, and microscopy imaging (transmission electron microscopy and atomic force microscopy) identified three different self-assembly regimes based on pH: (1) pH 2−5, positively charged, left-handed helical nanotubes; (2) pH 6−8, negatively charged, right-handed helical nanoribbons; and (3) pH ≥ 9.0, a monomeric/disassembled peptide. The nanotubes exhibited uniform diameters of 41 ± 5 nm and wall thicknesses of 4.8 ± 0.8 nm, whereas the nanoribbons existed as either flat or twisted sheets ranging in width from 11 to 60 nm with heights of 8 ± 1 nm. The UV−vis and CD spectra of the most common antiparallel, β-sheet conformation of **1**-dimer were simulated at the B3LYP/def2svpd level of theory in implicit water. These studies indicated that the transition from nanotubes to nanoribbons was coupled to an M → P helical inversion of the coumarin packing orientation, respectively, within the nanostructures. The assembly process was driven by β-sheet aggregation and π−π interactions, leading to the formation of nanoribbons, which progressively wound into helical ribbons and laterally grew into smooth nanotubes as the pH decreased.

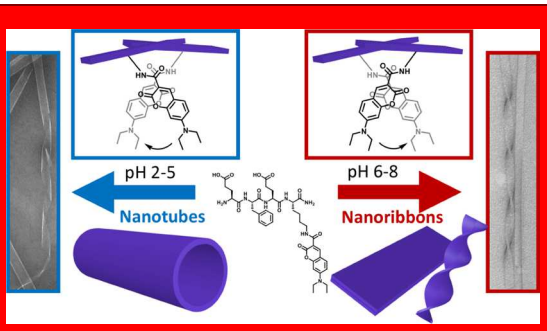

INTRODUCTION

The rational design of self-assembled nanostructures with controllable structural features represents a particularly important, albeit challenging, objective in the search for supramolecular function.[1,2] The importance of adaptable nanomaterials in biology[3−5] and energy conversion[6] emerges from the strong correlation relating the size, shape, and internal order of a nanostructure with the corresponding physical properties. In particular, small peptides derivatized with functional components[7] have the potential to self-assemble into nanoscale architectures with enhanced properties.[8] Responsive versions of these nanomaterials offer benefits to applications requiring a capability to respond to environmental changes or extrinsic inputs, such as optoelectronics,[9] sensors,[10] and biomedical devices.[11,12] Many self-assembled nanostructures undergo a hierarchical assembly process, such as the multistep assembly of β-sheet peptides into amyloid fibrils,[13] whereby local intermolecular order propagates to the ultimate nanostructure via progressively larger intermediate structures. Control over the final architecture of the assembly requires an understanding of the factors that permit one level of assembly to propagate to the next hierarchical stage.

Peptide self-assembly is controlled by a complex interplay of competing noncovalent interactions, such as π−π, hydrogen-bonding, electrostatic, and steric interactions. Amyloid peptides offer convenient access to a wide array of nanostructure morphologies, such as fibers,[14] ribbons,[15] tubes,[16] particles,[17] and vesicles.[18] The dynamic nature of the noncovalent interactions that drive self-assembly, and their susceptibility to extrinsic influences, enables responsiveness to stimuli such as temperature,[19−21] solvent,[22] additives,[23,24] light,[25−27] and pH.[28−32] Modulating the extent of interpeptide electrostatic repulsion via control of pH often leads to changes in β-sheet pitch[33] and, ultimately, the helical twisting of fibrils.[34,35] Thus, pH variation has been used to initiate self-assembly/disassembly,[36] to interconvert nanostructure morphology,[37] and to invert the helicity of twisted fibrils because of the differences in local packing chirality.[38,39] The helical arrangement of molecules within an ensemble often serves as a critical determinant of the final pathway taken by an assembly process,[22,28] suggesting the importance of local helical inversion as an important consideration for the design of adaptable nanomaterials.[2,19,24,25,38,40] Although these prior studies have been mostly limited to natural peptide sequences,

Received: June 25, 2019
Revised: August 29, 2019
Published: August 30, 2019

DOI: 10.1021/acs.langmuir.9b01939
Langmuir 2019, 35, 12460−12468

Scheme 1. Notional Depiction of the pH Dependence of the β-Sheet Self-Assembly of 1, into Nanotubes and Nanoribbons with Opposite Helical Packing

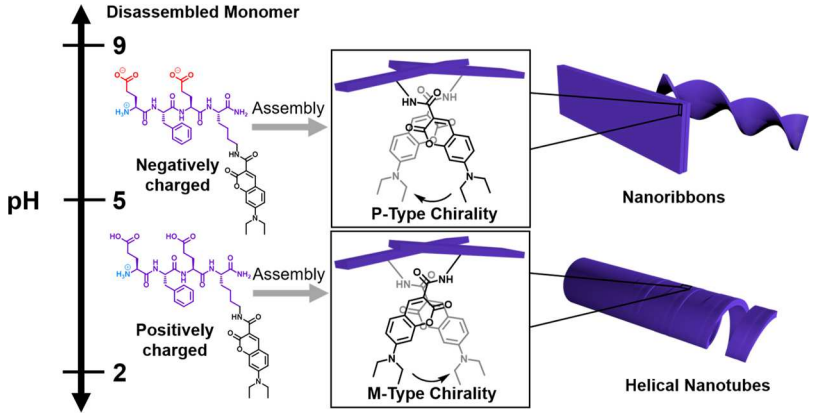

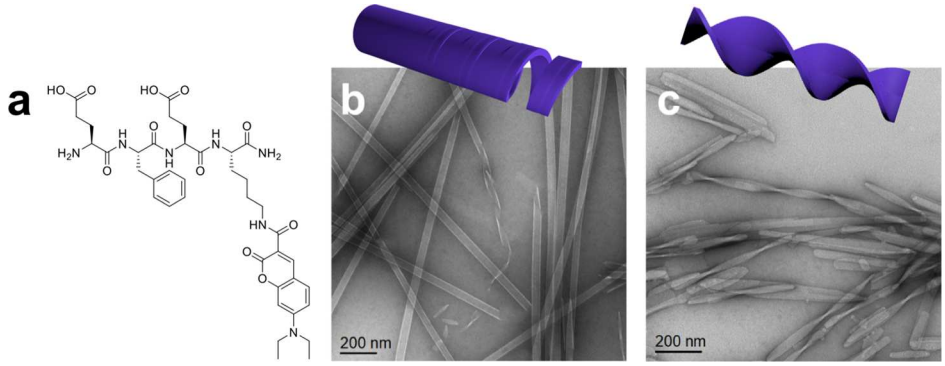

Figure 1. (a) Molecular structure of EFEK(DAC)−NH_2 (**1**); representative TEM images of (b) nanotubes, aged at 1 mM pH 4.0 at room temperature for 24 h, and (c) twisted and flat ribbons, aged at 0.5 mM pH 6.6 at room temperature for 24 h (deposited on a carbon-coated copper grid for 1 min and then exposed to 2% (w/w) uranyl acetate as a negative stain for 30 s).

the design of stimuli-responsive peptide nanomaterials with synthetic components will be necessary to realize the full potential of peptide-based nanomaterials.[41,42]

Coumarins represent an important class of compounds that have been shown to exhibit antioxidant, antihyperglycemic, and neuroprotective properties.[43,44] In conjunction with a program directed at creating nanostructures functionalized with non-natural side chains for potential biomedical applications, we explored the pH-dependent self-assembly of a tetrapeptide with a coumarin-modified side chain. This work shows how pH variation interconverts nanotubes and nanoribbons by initially inverting the helicity of intermolecular packing of the coumarin side chains within the assemblies, which further propagates to the macroscopic helicity of the assembled nanostructures (Scheme 1).

EXPERIMENTAL SECTION

Synthesis of Tetrapeptide 1 by Solid-Phase Peptide Synthesis. The tetrapeptide was manually prepared using fluorenylmethyloxycarbonyl (Fmoc) solid-phase peptide synthesis on rink amide resin (loading 0.8 mmol/g) (Scheme S1). Amide-coupling steps were accomplished with standard techniques for all amino acids: Fmoc−amino acid, 1,3-diisopropylcarbodiimide, and 1-hydroxybenzotriazole (HOBt); or HOBt, 2-(1*H*-benzotriazol-1-yl)-1,1,3,3-tetramethyluronium hexafluorophosphate (HBTU), and diisopropylamine (DIPEA) (3 equiv each relative to resin) in dimethylformamide (DMF) for 2 h. The 7-(*N*,*N*-diethylamino)coumarin-3-carboxylic acid[45] was coupled as the final step after the peptide chain was complete. After deprotection of the 4-methyltrityl (Mtt) group with 1% trifluoroacetic acid (TFA) in dichloromethane, 7-(*N*,*N*-diethylamino)coumarin-3-carboxylic acid was coupled to the peptide using standard peptide coupling conditions (DIPEA, HOBt, HBTU, and DMF). A solution of 20% piperidine in DMF was used for Fmoc removal. The final tetrapeptide conjugates were cleaved from the resin by the treatment with TFA/triethylsilane/water (94/5/1) at room temperature for 2 h. The crude peptides were precipitated with diethyl ether and purified by reverse-phase high-performance liquid chromatography on a preparative Waters XBridge C8 column, eluting with a linear gradient of CH_3CN/water containing 0.1% TFA (45−100% over 30 min) and then stored as lyophilized powders at 0 °C. ESI−MS: calcd for $C_{39}H_{51}N_7O_{11}$ $[M + H]^+$, 794.3719; found, 794.3735.

Sample Preparation of Nanotubes and Nanoribbons. Samples were prepared by suspending the purified solid of **1** in water to achieve the desired concentration (0.25−10 mM) and then adjusting the pH to 9.0 using aqueous 1 M NaOH, prior to the addition of sufficient aqueous 1 M HCl to reach pH 2−4 to form nanotubes or to pH 6−7 to form nanoribbons. Uniform distributions of the nanostructures, as observed by transmission electron microscopy (TEM) imaging, were optimally obtained at 0.25 mM for the nanotubes and 10 mM for nanoribbons (see the Supporting Information, Figure S10). The formation of nanotubes occurred immediately at pH 4.0 (0.25 mM), whereas nanoribbons formed more slowly over 24 h at pH 6.0 (10 mM).

Density Functional Theory Calculations. Four separate systems (*n*-butyl 7-*N*,*N*-diethylaminocoumarin-3-carboxamide, **1**-monomer at pH 9.0, **1**-monomer at pH 4.0, and **1**-dimer at pH 4.0) were optimized using a three-step protocol of a conformational search, low-level semiempirical (PM6) optimization, and a higher-level density functional theory (DFT) optimization at the B3LYP

DOI: 10.1021/acs.langmuir.9b01939
Langmuir 2019, 35, 12460−12468

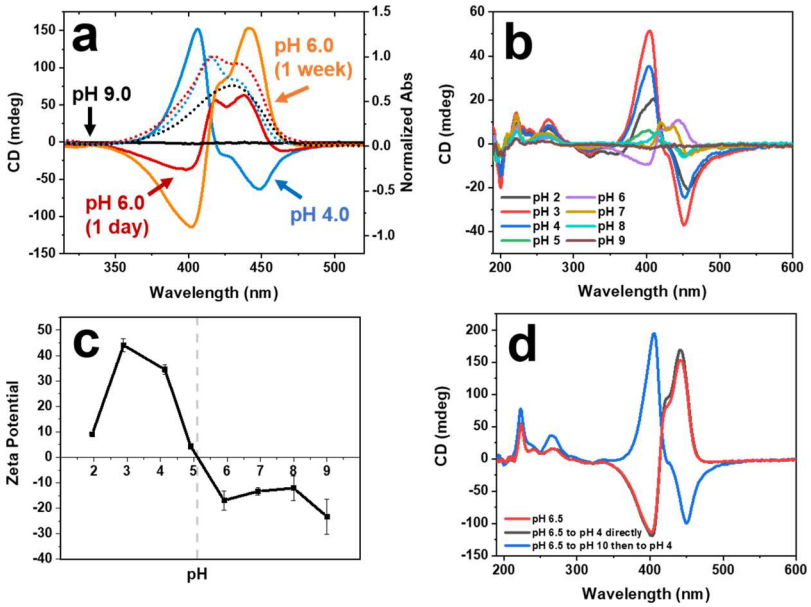

Figure 2. (a) CD spectra of **1** (0.25 mM), adjusted to pH 9.0 with aq NaOH (1 M) and then to pH 4.0, 6.0, and 9.0 with aq HCl (1 M) and aged 1 day (solid lines); pH 6.0 after aging for 1 week (orange line); and UV−vis spectra (dotted) at pH 4.0 (blue), pH 6.0 (red), and pH 9.0 (black). **1** (10 mM) was adjusted to pH 9.0 with aq NaOH (1 M) and then adjusted to pH 2−9 with aq HCl (1 M), aged 1 day at room temperature, and then diluted to 0.25 mM immediately for (b) pH dependence of CD spectroscopy, and (c) zeta potential measurements; (d) CD spectra of **1** (0.25 mM) aged for 1 week at pH 6.5 (red) and then adjusted to pH 4.0 with aq HCl (1 M) (black) or from pH 6.5 to pH 10.0 and then back down to pH 4.0 (blue) with CD spectra recorded within 5 min after adjusting the pH.

level of theory. This protocol was adapted from a recent report that studied supramolecular assemblies.[46] For each system, a suggested structure was constructed, and an exhaustive conformational analysis was performed to generate 20 different starting conformations with the OPLS3e force field[47] using the Macromodel package of Schrodinger 18.[48] The top 20 conformations were first subjected to a ground-state geometry optimization with a low-level semiempirical method, PM6.[49] The ground-state geometry optimizations were then carried out with the B3LYP[50−52] density functional with the def2svp basis set.[53] Solvent effects were simulated in water with the solvation model density method with electrostatics in terms of the integral equation formalism polarizable continuum model (IEF-PCM).[54−57] All ground-state geometry optimizations were performed with Gaussian 16.[58] The stationary points from these efforts were then carried on to the subsequent UV−vis studies.

Time-Dependent DFT Calculations. Simulated UV−vis and circular dichroism (CD) spectra were generated for each system. Single-point time-dependent (TD)-DFT calculations for all of the previously optimized conformations (B3LYP/def2svp) from the 20 starting geometries were taken at the B3LYP/def2svpd[50−53,59] level of theory and with the same solvent model in water with Gaussian 16.[58] However, Gaussian 16 does not have def2svp basis set with diffuse orbitals (def2-svpd), so it was loaded as a general basis set for C, N, O, and H atoms from the basis set exchange web service.[60,61] Single-point energy calculations were performed at the B3LYP/def2svpd[50−53,59] level of theory in order to measure the UV−vis spectra on the basis of the computed Boltzmann distribution.

RESULTS AND DISCUSSION

We prepared a tetrapeptide (EFEK(DAC)−NH_2, **1**, Figure 1a) with a 7-(*N*,*N*-diethylamino)-3-coumarin carboxamide (DAC) appended to the lysine side chain. The peptide sequence contained two glutamate residues and an N-terminal amine, which permitted the overall peptide charge to be tuned by pH variation as a method to modulate the electrostatic interactions between the peptide chains within a β-sheet assembly. Imaging of **1** by TEM over a pH range of 2−9 in water revealed that at low pH (2−5), nanotubes were formed with highly uniform diameters (41 ± 5 nm) and wall thicknesses (4.8 ± 0.8 nm), as shown in Figure 1b. In contrast, nanoribbons were observed in a pH range of 6−8 that were either flat or right-handed helices with varied widths of 11−60 nm (TEM) (Figure 1c) and heights of 8 ± 1 nm by atomic force microscopy (AFM), as shown in the Supporting Information (Figure S5). The lack of any observable structures by TEM in addition to a flat CD spectrum at pH ≥ 9.0 (Figure 2a) was consistent with a monomeric state for the peptide at this pH (Figure S6).

On the basis of these studies, three different self-assembly regimes could be identified: (1) pH 2−5, nanotubes, (2) pH 6−8, helical nanoribbons, and (3) pH ≥ 9 monomeric **1** (Scheme 1). These assembly regimes originated from changes in the protonation state of the molecule as the pH of the sample varied. The acid titration curve (Figure S7), coupled with the identification of the isoelectric point from zeta potential measurements (Figure 2c), indicated that **1** serves as at least a triprotic acid in the pH range from 2 to 10, with apparent pK_a values of 9.8 (pK_{a1}), 6.6 (pK_{a2}), and 3.2 (pK_{a3}), and an isoelectric pH of ∼5.0 (pI). The experimental lack of blue-shifting in the UV−vis spectrum of *n*-butyl-7-(*N*,*N*-diethylamino)coumarin-3-carboxamide at pH 2.0, as predicted computationally for protonation of the 7-(*N*,*N*-diethylamino) group (Figure S23), suggests that the coumarin side chain remains neutral at pH values above 2.0.[62] Accordingly, the value of pK_{a1} likely corresponds to the N-terminal ammonium group, whereas pK_{a2} and pK_{a3} reflect both glutamate side chains. Therefore, as the pH approached pK_{a3}, the peptide would maintain a formal charge of +1, which was reflected as a positive zeta potential. However, at pH values near pK_{a2}, a formal charge of −1 resulted in a negative zeta potential (Figure 2c). These opposite charge states of the peptide resulted in left-handed helical nanotubes and right-handed helical nanoribbons, respectively. In contrast, the increased electrostatic repulsion that accompanied a formal charge of −2

DOI: 10.1021/acs.langmuir.9b01939
Langmuir 2019, 35, 12460−12468

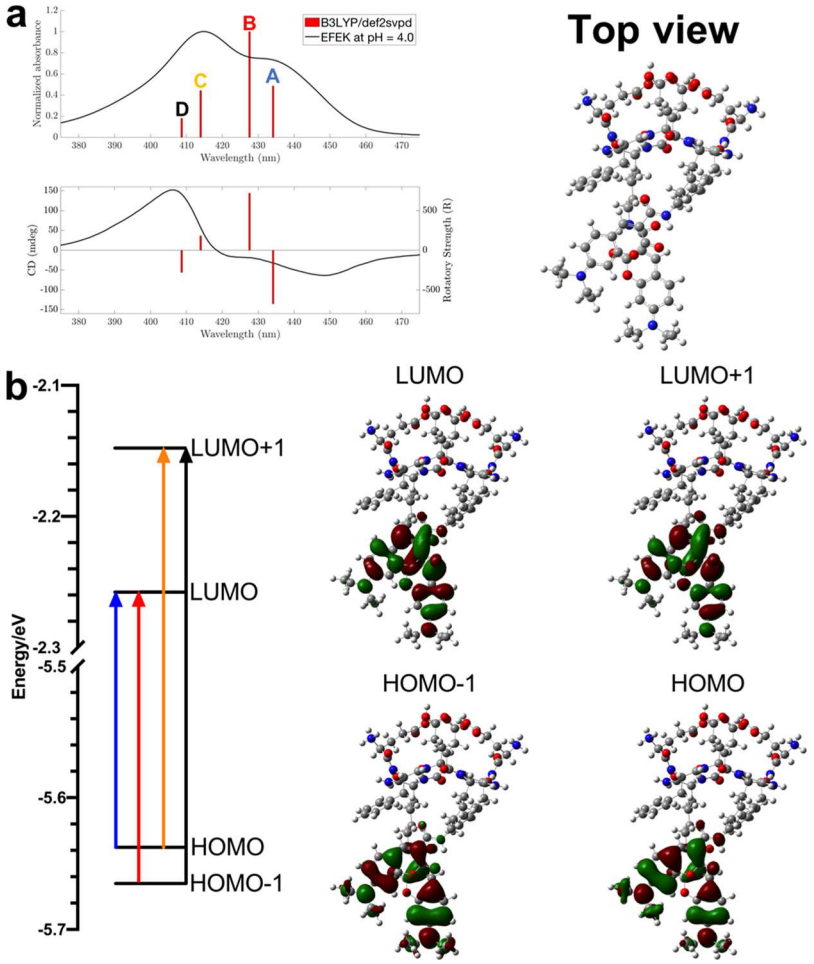

Figure 3. (a) Simulated UV−vis and CD spectra at the B3LYP/def2svpd level of theory in implicit water of the most common antiparallel conformation of **1** dimer at a pH of 4.0 with four separate $\pi-\pi^*$ transitions A (blue), B (red), C (orange), and D (black). (b) HOMO − 1, HOMO, LUMO, and LUMO + 1 orbitals of the dimer and the orbitals with the largest contribution to each excitation, as color coded for each transition.

for the peptide at pH ≥ 9 dissociated the assemblies into a monomeric state.

These nanostructures were further characterized by CD, absorption (UV−vis), and Fourier transform infrared (FT-IR) spectroscopy to evaluate the impact of pH on the self-assembly process. Amide I FT-IR bands indicative of a β-sheet secondary structure were observed at 1629, 1628, and 1628 cm^{-1} in the IR spectra at pH 2.0, 4.0, and 6.0, respectively (Figure S17a−c).[63] At higher pH values of 8.1 and 11.0, the 1628−1629 cm^{-1} peaks were significantly reduced relative to new bands at 1648−1649 and 1612−1616 cm^{-1}, attributed to a random coil peptide structure and to the coumarin moiety, respectively (Figure S17d−f). The UV−vis absorption spectrum of **1**, in water (0.25 mM) at pH 9.0, displayed a broad absorption maximum at 430 nm (Figures 2a and S21), which corresponded to a $\pi-\pi^*$ transition with the transition dipole along the long axis of the coumarin chromophore.[64] The silent CD spectrum at pH ≥ 9.0 was indicative of a monomeric state for the peptide (Figures 2a and S6). Decreasing the pH from 9.0 to 6.0 or 4.0 splits the absorption into a blue-shifted peak at 415 nm and a shoulder at ∼435 nm (Figures 2a and S21).[64,65]

Steady-state fluorescence measurements of **1** at pH 4.0 (25 μM) exhibited emission spectra with λ_{max}^{Fl} values that were nearly independent of the excitation values in the range of 400−450 nm (Figure S18). Normalized fluorescence excitation spectra probed over various emission wavelengths were relatively invariant and in excellent agreement with the UV−vis spectra of **1**. Although the low concentrations required to obtain emission spectra were not optimal for nanotube formation, these spectra suggested that the two split peaks at 415 and 435 nm emerged from a single assembled species.[66] To provide additional insight about the absorption properties, peptide **1** was computationally modeled as an antiparallel, β-sheet dimer with a formal charge of +1 on each peptide strand because of protonation of the N-terminal amines at pH 4.0 (Scheme 1). TD-DFT calculations of 20 different conformations of the antiparallel dimer revealed four different $\pi-\pi^*$ transitions that contributed to the broad UV−vis spectra of **1** at pH 4.0. Analysis of these transitions indicated that the observed splitting emerged from excitonic delocalization of highest occupied molecular orbital (HOMO) and lowest unoccupied molecular orbital (LUMO) orbitals on the coumarins from adjacent coumarin moieties within the β-sheet dimers. The peaks of the highest intensity were derived from HOMO and HOMO − 1 to LUMO and LUMO + 1 transitions in the dimer (Figure 3a; excitations A and B). Modeling of monomeric **1** in the same protonation state produced only one $\pi-\pi^*$ transition, suggesting that the two split peaks were produced by excitonic coupling of the

DOI: 10.1021/acs.langmuir.9b01939
Langmuir 2019, 35, 12460−12468

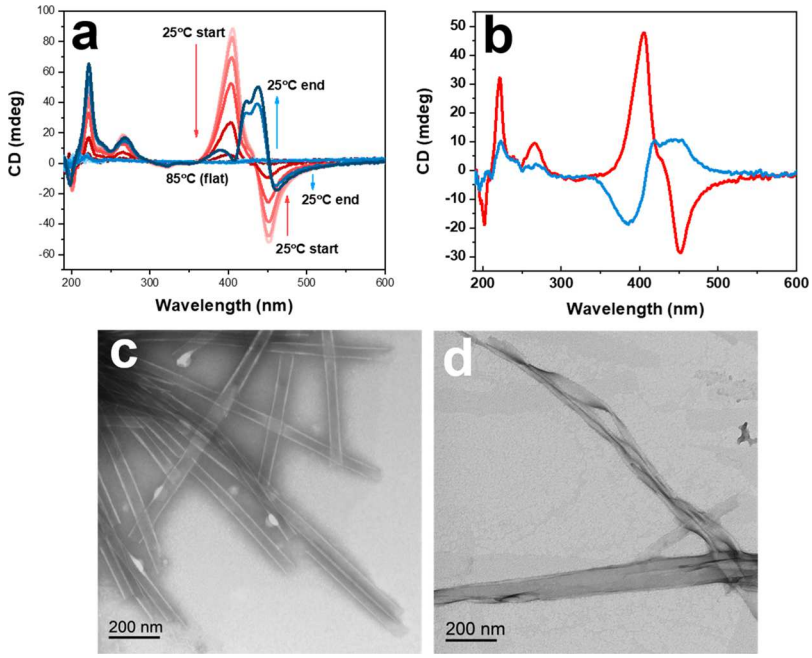

Figure 4. CD spectra of **1** at pH 4.0 (a) as the temperature was increased from 25 to 85 °C and then back to 25 °C with measurements taken in intervals of 10 °C and a temperature gradient of 5 °C per minute; (b) before (red) and after (blue) heating sample **1** at pH 4.0 for two cycles; (c) TEM image of **1** at pH 4.0, displaying nanotubes, corresponding to the red CD spectrum in (b); and (d) TEM image of **1** at pH 4.0, displaying nanoribbons, corresponding to the blue CD spectrum in (b). The concentration of **1** in all samples was 0.25 mM.

coumarin transitions within the β-sheet aggregates (Figures S28–S31).

Correspondingly, the ~350–480 nm region of the CD spectra exhibited bisignate peaks that varied in sign and shape, depending on pH, concentration, and time. For example, a sample of **1**, initially at pH ≥ 9.0 (10 mM) showing a flat CD signal, was adjusted to pH 6.0 to assemble the nanoribbons. After diluting to 0.25 mM, this sample displayed two positive peaks at 418 and 437 nm and a negative peak at 397 nm (Figure 2a). Performing the same sequence going from pH ≥ 9.0 to pH 4.0, in order to assemble the nanotubes, produced a nearly inverted spectrum with negative peaks at 426 and 448 nm and a positive peak at 405 nm. Although the spectrum of the nanotubes at pH 4.0 appeared immediately as shown in Figure 2a and did not change over time, the nanoribbons formed at pH 6–7 (Figure 2a,b) produced a CD signal that progressively changed over 1 week at 0.25 mM to become the mirror image of the spectrum at pH 4.0 (see Figure 2a red and orange). The CD spectrum observed at pH 4.0 could be attributed to a negative excitonic couplet with a zero-crossing at ~415 nm along with an additional negative peak at 448 nm, which likely emerged from the contribution of a slightly different conformation of **1** within the assembled nanostructure (Figures S37–S40). The couplets in this region of the CD spectra emanate from π–π^* transitions containing electric transition moments that run along the long axis of the coumarin chromophore.[67] Therefore, the negative couplet at pH 4.0 indicated that the coumarin chromophores were packed with an M-type helical twist sense within the nanotubes (Scheme 1). In contrast, the inverted CD spectra at pH 6.0 were due to the presence of positive excitonic couplets, reflecting a P-type helical twist sense of the coumarin chromophores within the nanoribbons (Scheme 1). Computational modeling of the CD spectrum of **1**-dimer at pH 4.0 revealed that the M-type couplet was a result of a change in the symmetry of nearly degenerate HOMO and HOMO − 1 molecular orbitals (Figure 3). The peaks of the highest intensity were derived from the HOMO and HOMO − 1 to LUMO π–π^* transitions in the CD and displayed an M-type excitonic couplet in the calculated CD spectrum. Modeling of the monomer of **1** in a protonation state reflecting a formal charge of −2 for a pH value of 9.0 did not reveal either the observed UV–vis splitting or the CD excitons (Figures S28–S31).

Zeta potential measurements of **1**, recorded over a pH range of 2–9 (after aging for 24 h at each pH value) indicated the presence of an isoelectric pH at ~5, with positive and negative surface potentials below and above that pH value, respectively (Figure 2c). Progressively adjusting the pH from 9.0 to 2.0 showed that the helicity inversion occurred at pH ~5.0, that is, the isoelectric pH, as the molecular charge of **1** transitioned from negative to positive (Figure 2b). A close inspection of the TEM images at pH 4.0 indicated that the nanotubes were formed by left-hand helical coiling of a ribbon, suggesting that the M-type packing of the monomers propagated to the macroscopic twisting of the nanotube (Figures 1b and S12a). Similarly, the nanoribbons formed at pH 6.0 were either flat or twisted with a right-handed helicity, corresponding to the P-type helical packing of the monomers (Figures 1c and S12b). However, the underlying factors that determine the twist of supramolecular structures are complex.[68] Although amino acid chirality usually correlates with nanofibril twist sense in amyloid peptides,[69] an unequivocal rationale for macroscopic chirality is complicated by the fact that the structure,[70] chirality,[71,72] or charge[33] of terminal residues of the peptide and even pH[73] have been shown to greatly impact the macroscopic handedness of the nanostructure.

The rate of interconversion between the nanotubes and nanoribbons was also affected by variables such as concentration, temperature, and the starting aggregation state of **1**.

DOI: 10.1021/acs.langmuir.9b01939
Langmuir 2019, 35, 12460–12468

For example, although the CD spectrum at pH 4.0, corresponding to the formation of nanotubes, reached maximal intensity within 1 day, the nanoribbons formed at pH 6.0 produced a CD spectrum that progressively increased in amplitude [Figures 2a (red and orange) and S10e] and exhibited an increasingly organized structure by TEM over ∼1 week (Figure S13). Imaging by TEM also showed that nanotubes formed at low concentration (0.25 mM) were significantly more uniform than at higher concentrations (10 mM), whereas higher concentrations were optimal to form the nanoribbons (Figure S10a−d). Furthermore, the nanotubes could be converted into the nanoribbons at pH 4.0 by heating (Figure 4a).[74] As shown in Figure 4a, exposing a sample of **1** (0.25 mM, pH 4.0, nanotubes) to two heating/cooling cycles from 25 to 85 °C resulted in a nearly inverted CD spectrum (Figure 4a,b), and corresponding TEM images showed conversion to a nanoribbon morphology (Figure 4c,d). In comparison, heating and cooling a sample of nanoribbons did not have any effect on their morphologies or CD spectra (Figure S9). Monitoring the pH of the solutions as the nanotubes formed by **1** at pH 3.0 were exposed to two cycles of heating at 80 °C for 15 min, followed by cooling for 15 min, revealed that the thermal transition to a nanoribbon morphology was accompanied by a concomitant increase in pH to ∼6.0 (Figure S15a,b). Conversely, maintaining the solution pH to ≤5 throughout each heating/cooling cycle prevented conversion to nanoribbons, as indicated by CD and TEM imaging (Figure S15c,d). These experiments suggested that the thermodynamic position of the nanoribbon−nanotube interconversion strongly depended on the solution pH, and the corresponding charge state of the peptide.

The interconversion rate was greatly facilitated by dissociating the nanostructures at pH ≥ 9.0, prior to adjusting to pH 6.0 or 4.0. For example, in Figure 2d, a pH 6.5 sample of nanoribbons showed no immediate change in the CD spectrum upon adjustment to pH 4.0; however, when the sample was adjusted to pH ≥ 9.0 and then to pH 4.0, nanotube formation was apparent by CD after 5 min. These observations indicated that the interconversion between the two morphological states was hampered in the self-assembled state. Tight packing of the monomers in the assembled state would suppress the molecular reorganization, such as the M → P inversion in packing helicity, required to interconvert the nanostructures. Thus, each nanostructure would be expected to self-assemble more rapidly from the monomeric state than from an assembled state.

A proposed model for the assembly behavior of **1** is presented in Scheme 1. FT-IR spectroscopy and computational modeling indicated that self-assembly was driven by β-sheet self-assembly in addition to the $\pi-\pi$ stacking of the coumarin side chain, as evidenced by CD and UV−vis spectra. The variations in formal charge as a function of pH alter the nature of the electrostatic repulsions within the β-sheet aggregates, forcing the peptide molecules to interact with different relative helical orientations, which were propagated to different nanostructure morphologies.[39,75] Thus, the sense of local intermolecular and macroscopic helical twisting, and ultimately the structure of the assembly, could be dynamically controlled by pH variation. The extended length (2.35 nm) of **1** (Figure S36) and the measured width of the nanotube walls by TEM imaging (4.81 ± 0.8 nm) were consistent with a bilayer structure for the nanotube walls. The height of the flat and twisted ribbons varied from 5 to 9 nm by AFM because of the presence of multiple sheets stacked together and helical twisting, with the flat segments measuring an average of 7.98 ± 1 nm (Figure S5). The nanotube assembly process could be attributed to initial formation of a bilayer nanoribbon composed of two stacked, β-sheet aggregates of **1**, which then progressively coiled into the nanotube structure as the pH was decreased. Consistent with amyloid β-sheet assembly, the bilayer could be expected to sequester the hydrophobic coumarin and phenylalanine side chains of **1** toward the interior with the more hydrophilic glutamic acid side chains projected toward the aqueous interface.[76] TEM images, with the corresponding CD spectra of intermediates, were recorded at early time points of the interconversion between the nanotube and nanoribbon morphologies to elucidate the mechanism of assembly/interconversion process (Figure S16). These images showed flat ribbon-type structures protruding from the nanotube ends 12 h after changing the pH of a sample of fully formed nanoribbons (0.25 mM) from 4.3 to 7.5. Similar intermediate structures were observed 30 min after changing the pH of nanoribbons (0.25 mM) from 6.9 to 3.0. On the basis of these observations, the interconversion between the left-handed nanotubes and the right-handed nanoribbons likely proceeded via an initial unwinding of the nanotubes into flat ribbon structures followed by the formation of right-handed nanoribbons.

CONCLUSIONS

In summary, our results showed that coumarin−peptide **1** experienced a polymorphic self-assembly process that was primarily driven by peptide β-sheet interactions and the $\pi-\pi$ stacking of coumarin side chains. The morphology of the nanostructure could be controlled by changes in pH, which altered both interpeptide electrostatic interactions and the chirality of coumarin $\pi-\pi$ stacking. On the basis of pK_a and zeta potential measurements, the formally negative charge of the peptide at pH values above the isoelectric pH (pI 5.0) resulted in the formation of nanoribbons composed of P-helically packed coumarin chromophores. However, at pH ≥ 9, the increased electrostatic repulsions dissociated the nanoribbons into a monomeric state of the peptide. At low pH values below the isoelectric pH, the formally positive peptide assembled with the coumarins packed with M-type chirality, leading to the formation of well-defined nanotubes. Moreover, the relative stability of the nanoribbons, compared with that of the nanotubes, was highly dependent on pH. Thus, annealing experiments where the nanotubes efficiently transitioned into the nanoribbons upon exposure to heating/cooling cycle were accompanied by an increase in pH to ∼6. In contrast, a similar treatment of the nanoribbons under conditions that maintained the pH below 5 produced no changes. Because of the intermolecular reorganization needed to interconvert between the nanostructures, the tight packing of the monomers within the assembled states hampered the rate of interconversion. Thus, starting from the monomeric states at pH ≥ 9.0 accelerated the self-assembly of either morphological state. This knowledge provides insight into the design and control of chiral properties of nanomaterials produced from small, optically active peptides, which could lead to the development of environmentally adaptable nanomaterials for use in optoelectronics or biomedical devices.

DOI: 10.1021/acs.langmuir.9b01939
Langmuir 2019, 35, 12460−12468

■ ASSOCIATED CONTENT

Supporting Information

The Supporting Information is available free of charge on the ACS Publications website at DOI: 10.1021/acs.langmuir.9b01939.

TEM, AFM, UV, emission, and CD data of **1**; and computational results for the geometries, energies, TD-DFT, and CD results (PDF)

■ AUTHOR INFORMATION

Corresponding Author

*E-mail: parquette.1@osu.edu.

ORCID

Jon R. Parquette: 0000-0002-4803-028X

Author Contributions

This manuscript was written through contributions from all authors. All authors have given approval to the final version of the manuscript.

Funding

This work was supported by the National Science Foundation (CHE-1708390 and CHE-1708388).

Notes

The authors declare no competing financial interest.

■ ACKNOWLEDGMENTS

The authors acknowledge the technical assistance and usage of the AFM facility at the Ohio State Surface Analysis Lab. The TEM images shown were generated at the Campus Microscopy and Imaging Facility at The Ohio State University. This facility is supported in part by grant NIH P30 CA016058, National Cancer Institute, Bethesda, MD. The authors acknowledge the generous computational resources provided by the Ohio Supercomputer Center.

■ REFERENCES

(1) Blum, A. P.; Kammeyer, J. K.; Rush, A. M.; Callmann, C. E.; Hahn, M. E.; Gianneschi, N. C. Stimuli-responsive nanomaterials for biomedical applications. *J. Am. Chem. Soc.* **2015**, *137*, 2140−2154.

(2) Goskulwad, S.; La, D. D.; Kobaisi, M. A.; Bhosale, S. V.; Bansal, V.; Vinu, A.; Ariga, K.; Bhosale, S. V. Dynamic multistimuli-responsive reversible chiral transformation in supramolecular helices. *Sci. Rep.* **2018**, *8*, 11220.

(3) Park, W.; Na, K. Advances in the synthesis and application of nanoparticles for drug delivery. *Wiley Interdiscip. Rev.: Nanomed. Nanobiotechnol.* **2015**, *7*, 494−508.

(4) Samanta, A.; Medintz, I. L. Nanoparticles and DNA - a powerful and growing functional combination in bionanotechnology. *Nanoscale* **2016**, *8*, 9037−9095.

(5) Castellana, M.; Wilson, M. Z.; Xu, Y.; Joshi, P.; Cristea, I. M.; Rabinowitz, J. D.; Gitai, Z.; Wingreen, N. S. Enzyme clustering accelerates processing of intermediates through metabolic channeling. *Nat. Biotechnol.* **2014**, *32*, 1011−1018.

(6) Zhang, Q.; Uchaker, E.; Candelaria, S. L.; Cao, G. Nanomaterials for energy conversion and storage. *Chem. Soc. Rev.* **2013**, *42*, 3127−3171.

(7) Hamley, I. W. Small Bioactive Peptides for Biomaterials Design and Therapeutics. *Chem. Rev.* **2017**, *117*, 14015−14041.

(8) Knowles, T. P. J.; Mezzenga, R. Amyloid Fibrils as Building Blocks for Natural and Artificial Functional Materials. *Adv. Mater.* **2016**, *28*, 6546−6561.

(9) Kuzyk, A.; Schreiber, R.; Fan, Z.; Pardatscher, G.; Roller, E.-M.; Högele, A.; Simmel, F. C.; Govorov, A. O.; Liedl, T. DNA-based self-assembly of chiral plasmonic nanostructures with tailored optical response. *Nature* **2012**, *483*, 311−314.

(10) Zou, W.; Yan, Y.; Fang, J.; Yang, Y.; Liang, J.; Deng, K.; Yao, J.; Wei, Z. Biomimetic superhelical conducting microfibers with homochirality for enantioselective sensing. *J. Am. Chem. Soc.* **2014**, *136*, 578−581.

(11) Kim, S. H.; Kaplan, J. A.; Sun, Y.; Shieh, A.; Sun, H.-L.; Croce, C. M.; Grinstaff, M. W.; Parquette, J. R. The self-assembly of anticancer camptothecin-dipeptide nanotubes: a minimalistic and high drug loading approach to increased efficacy. *Chem.—Eur. J.* **2015**, *21*, 101−105.

(12) Liu, G.-F.; Zhang, D.; Feng, C.-L. Control of three-dimensional cell adhesion by the chirality of nanofibers in hydrogels. *Angew. Chem.* **2014**, *53*, 7789−7793.

(13) Aggeli, A.; Nyrkova, I. A.; Bell, M.; Harding, R.; Carrick, L.; McLeish, T. C. B.; Semenov, A. N.; Boden, N. Hierarchical self-assembly of chiral rod-like molecules as a model for peptide beta -sheet tapes, ribbons, fibrils, and fibers. *Proc. Natl. Acad. Sci. U.S.A* **2001**, *98*, 11857−11862.

(14) Wagner, D. E.; Phillips, C. L.; Ali, W. M.; Nybakken, G. E.; Crawford, E. D.; Schwab, A. D.; Smith, W. F.; Fairman, R. Toward the development of peptide nanofilaments and nanoropes as smart materials. *Proc. Natl. Acad. Sci. U.S.A* **2005**, *102*, 12656−12661.

(15) Castelletto, V.; Hamley, I. W.; Hule, R. A.; Pochan, D. Helical-Ribbon Formation by a beta-Amino Acid Modified Amyloid beta-Peptide Fragment. *Angew. Chem. Int. Ed.* **2009**, *48*, 2317−2320.

(16) Mehta, A. K.; Lu, K.; Childers, W. S.; Liang, Y.; Dublin, S. N.; Dong, J.; Snyder, J. P.; Pingali, S. V.; Thiyagarajan, P.; Lynn, D. G. Facial symmetry in protein self-assembly. *J. Am. Chem. Soc.* **2008**, *130*, 9829−9835.

(17) Orbach, R.; Adler-Abramovich, L.; Zigerson, S.; Mironi-Harpaz, I.; Seliktar, D.; Gazit, E. Self-Assembled Fmoc-Peptides as a Platform for the Formation of Nanostructures and Hydrogels. *Biomacromolecules* **2009**, *10*, 2646−2651.

(18) Vauthey, S.; Santoso, S.; Gong, H.; Watson, N.; Zhang, S. Molecular self-assembly of surfactant-like peptides to form nanotubes and nanovesicles. *Proc. Natl. Acad. Sci. U.S.A* **2002**, *99*, 5355−5360.

(19) Kumar, J.; Nakashima, T.; Kawai, T. Inversion of supramolecular chirality in bichromophoric perylene bisimides: influence of temperature and ultrasound. *Langmuir* **2014**, *30*, 6030−6037.

(20) Miravet, J. F.; Escuder, B.; Segarra-Maset, M. D.; Tena-Solsona, M.; Hamley, I. W.; Dehsorkhi, A.; Castelletto, V. Self-assembly of a peptide amphiphile: transition from nanotape fibrils to micelles. *Soft Matter* **2013**, *9*, 3558−3564.

(21) Zhang, S.; Greenfield, M. A.; Mata, A.; Palmer, L. C.; Bitton, R.; Mantei, J. R.; Aparicio, C.; de la Cruz, M. O.; Stupp, S. I. A self-assembly pathway to aligned monodomain gels. *Nat. Mater.* **2010**, *9*, 594−601.

(22) Li, Y.; Li, B.; Fu, Y.; Lin, S.; Yang, Y. Solvent-induced handedness inversion of dipeptide sodium salts derived from alanine. *Langmuir* **2013**, *29*, 9721−9726.

(23) Liu, J. Y.; Qin, M. G.; Auphedeous, D. I. Y.; Liu, Z. W.; Dou, X. Q.; Feng, C. L. Inversion of Supramolecular Chirality of Nanofibrous Structures Tuned by the Odd-Even Effects among Bis-amide and Bis-urea. *Acta Polym. Sin.* **2018**, 80−89.

(24) Liu, G.; Sheng, J.; Wu, H.; Yang, C.; Yang, G.; Li, Y.; Ganguly, R.; Zhu, L.; Zhao, Y. Controlling Supramolecular Chirality of Two-Component Hydrogels by J- and H-Aggregation of Building Blocks. *J. Am. Chem. Soc.* **2018**, *140*, 6467−6473.

(25) Kim, J.; Lee, J.; Kim, W. Y.; Kim, H.; Lee, S.; Lee, H. C.; Lee, Y. S.; Seo, M.; Kim, S. Y. Induction and control of supramolecular chirality by light in self-assembled helical nanostructures. *Nat. Commun.* **2015**, *6*, 6959.

(26) Muraoka, T.; Cui, H.; Stupp, S. I. Quadruple helix formation of a photoresponsive peptide amphiphile and its light-triggered dissociation into single fibers. *J. Am. Chem. Soc.* **2008**, *130*, 2946−2947.

(27) Matson, J. B.; Navon, Y.; Bitton, R.; Stupp, S. I. Light-Controlled Hierarchical Self-Assembly of Polyelectrolytes and Supramolecular Polymers. *ACS Macro Lett.* **2015**, *4*, 43−47.
(28) Sun, P.; Wu, A.; Sun, N.; Qiao, X.; Shi, L.; Zheng, L. Multiple-Responsive Hierarchical Self-Assemblies of a Smart Supramolecular Complex: Regulation of Noncovalent Interactions. *Langmuir* **2018**, *34*, 2791−2799.
(29) Chen, Y.; Gan, H. X.; Tong, Y. W. pH-Controlled Hierarchical Self-Assembly of Peptide Amphiphile. *Macromolecules* **2015**, *48*, 2647−2653.
(30) Qin, S.-Y.; Jiang, H.-F.; Peng, M.-Y.; Lei, Q.; Zhuo, R.-X.; Zhang, X.-Z. Adjustable nanofibers self-assembled from an irregular conformational peptide amphiphile. *Polym. Chem.* **2015**, *6*, 519−524.
(31) Tsonchev, S.; Niece, K. L.; Schatz, G. C.; Ratner, M. A.; Stupp, S. I. Phase diagram for assembly of biologically-active peptide amphiphiles. *J. Phys. Chem. B* **2008**, *112*, 441−447.
(32) Tena-Solsona, M.; Alonso-de Castro, S.; Miravet, J. F.; Escuder, B. Co-assembly of tetrapeptides into complex pH-responsive molecular hydrogel networks. *J. Mater. Chem. B* **2014**, *2*, 6192−6197.
(33) Hu, Y.; Lin, R.; Zhang, P.; Fern, J.; Cheetham, A. G.; Patel, K.; Schulman, R.; Kan, C.; Cui, H. Electrostatic-Driven Lamination and Untwisting of beta-Sheet Assemblies. *ACS Nano* **2016**, *10*, 880−888.
(34) Adamcik, J.; Jung, J.-M.; Flakowski, J.; De Los Rios, P.; Dietler, G.; Mezzenga, R. Understanding amyloid aggregation by statistical analysis of atomic force microscopy images. *Nat. Nanotechnol.* **2010**, *5*, 423−428.
(35) Adamcik, J.; Mezzenga, R. Adjustable twisting periodic pitch of amyloid fibrils. *Soft Matter* **2011**, *7*, 5437−5443.
(36) Tena-Solsona, M.; Alonso-de Castro, S.; Miravet, J. F.; Escuder, B. Co-assembly of tetrapeptides into complex pH-responsive molecular hydrogel networks. *J. Mater. Chem. B* **2014**, *2*, 6192−6197.
(37) Koc, M. H.; Ciftci, G. C.; Baday, S.; Castelletto, V.; Hamley, I. W.; Guler, M. O. Hierarchical Self-Assembly of Histidine-Functionalized Peptide Amphiphiles into Supramolecular Chiral Nanostructures. *Langmuir* **2017**, *33*, 7947−7956.
(38) Xie, Y.; Wang, Y.; Qi, W.; Huang, R.; Su, R.; He, Z. Reconfigurable Chiral Self-Assembly of Peptides through Control of Terminal Charges. *Small* **2017**, *13*, 1700999.
(39) Xie, Y.; Wang, X.; Huang, R.; Qi, W.; Wang, Y.; Su, R.; He, Z. Electrostatic and aromatic interaction-directed supramolecular self-assembly of a designed Fmoc-tripeptide into helical nanoribbons. *Langmuir* **2015**, *31*, 2885−2894.
(40) Lv, Z. Y.; Chen, Z. H.; Shao, K. N.; Qing, G. Y.; Sun, T. L. Stimuli-Directed Helical Chirality Inversion and Bio-Applications. *Polymers* **2016**, *8*, 310.
(41) Ulijn, R. V.; Smith, A. M. Designing peptide based nanomaterials. *Chem. Soc. Rev.* **2008**, *37*, 664−675.
(42) Ni, M.; Zhuo, S. Applications of self-assembling ultrashort peptides in bionanotechnology. *RSC Adv.* **2019**, *9*, 844−852.
(43) Yang, H.-L.; Cai, P.; Liu, Q.-H.; Yang, X.-L.; Li, F.; Wang, J.; Wu, J.-J.; Wang, X.-B.; Kong, L.-Y. Design, synthesis and evaluation of coumarin-pargyline hybrids as novel dual inhibitors of monoamine oxidases and amyloid-beta aggregation for the treatment of Alzheimer's disease. *Eur. J. Med. Chem.* **2017**, *138*, 715−728.
(44) Jiang, N.; Huang, Q.; Liu, J.; Liang, N.; Li, Q.; Li, Q.; Xie, S.-S. Design, synthesis and biological evaluation of new coumarin-dithiocarbamate hybrids as multifunctional agents for the treatment of Alzheimer's disease. *Eur. J. Med. Chem.* **2018**, *146*, 287−298.
(45) Ma, Y.; Luo, W.; Quinn, P. J.; Liu, Z.; Hider, R. C. Design, synthesis, physicochemical properties, and evaluation of novel iron chelators with fluorescent sensors. *J. Med. Chem.* **2004**, *47*, 6349−6362.
(46) Wehner, M.; Röhr, M. I. S.; Bühler, M.; Stepanenko, V.; Wagner, W.; Würthner, F. Supramolecular Polymorphism in One-Dimensional Self-Assembly by Kinetic Pathway Control. *J. Am. Chem. Soc.* **2019**, *141*, 6092−6107.
(47) Harder, E.; Damm, W.; Maple, J.; Wu, C.; Reboul, M.; Xiang, J. Y.; Wang, L.; Lupyan, D.; Dahlgren, M. K.; Knight, J. L.; Kaus, J. W.; Cerutti, D. S.; Krilov, G.; Jorgensen, W. L.; Abel, R.; Friesner, R. A. OPLS3: A Force Field Providing Broad Coverage of Drug-like Small Molecules and Proteins. *J. Chem. Theory Comput.* **2016**, *12*, 281−296.
(48) *Schrodinger Release 2018-3: Macromodel*; Schrodinger, LLC: New York, 2018.
(49) Stewart, J. J. P. Optimization of parameters for semiempirical methods V: Modification of NDDO approximations and application to 70 elements. *J. Mol. Model.* **2007**, *13*, 1173−1213.
(50) Becke, A. D. Density-functional thermochemistry. III. The role of exact exchange. *J. Chem. Phys.* **1993**, *98*, 5648−5652.
(51) Kim, K.; Jordan, K. D. Comparison of Density Functional and MP2 Calculations on the Water Monomer and Dimer. *J. Phys. Chem.* **1994**, *98*, 10089−10094.
(52) Stephens, P. J.; Devlin, F. J.; Chabalowski, C. F.; Frisch, M. J. Ab Initio Calculation of Vibrational Absorption and Circular Dichroism Spectra Using Density Functional Force Fields. *J. Phys. Chem.* **1994**, *98*, 11623−11627.
(53) Weigend, F.; Ahlrichs, R. Balanced basis sets of split valence, triple zeta valence and quadruple zeta valence quality for H to Rn: Design and assessment of accuracy. *Phys. Chem. Chem. Phys.* **2005**, *7*, 3297.
(54) Miertuš, S.; Scrocco, E.; Tomasi, J. Electrostatic interaction of a solute with a continuum. A direct utilizaion of AB initio molecular potentials for the prevision of solvent effects. *Chem. Phys.* **1981**, *55*, 117−129.
(55) Miertuš, S.; Tomasi, J. Approximate evaluations of the electrostatic free energy and internal energy changes in solution processes. *Chem. Phys.* **1982**, *65*, 239−245.
(56) Pascual-ahuir, J. L.; Silla, E.; Tuñon, I. GEPOL: An improved description of molecular surfaces. III. A new algorithm for the computation of a solvent-excluding surface: GEPOL. *J. Comput. Chem.* **1994**, *15*, 1127−1138.
(57) Marenich, A. V.; Cramer, C. J.; Truhlar, D. G. Universal Solvation Model Based on Solute Electron Density and on a Continuum Model of the Solvent Defined by the Bulk Dielectric Constant and Atomic Surface Tensions. *J. Phys. Chem. B* **2009**, *113*, 6378−6396.
(58) Frisch, M. J.; Trucks, G. W.; Schlegel, H. B.; Scuseria, G. E.; Robb, M. A.; Cheeseman, J. R.; Scalmani, G.; Barone, V.; Petersson, G. A.; Nakatsuji, H.; Li, X.; Caricato, M.; Marenich, A. V.; Bloino, J.; Janesko, B. G.; Gomperts, R.; Mennucci, R.; ian, H. P.; Ortiz, D. V.; Izmaylov, A. F.; Sonnenburg, J. L.; Williams-Young, D.; Ding, F.; Lipparini, F.; Egidi, F.; Goings, J.; Peng, B.; Petrone, A.; Henderson, T.; Ranasinghe, D.; Zakrzewski, V. G.; Gao, J.; Rega, N.; Zheng, G.; Liang, W.; Hada, M.; Ehara, M.; Toyota, K.; Fukuda, R.; Hasegawa, J.; Ishida, M.; Nakajima, T.; Honda, Y.; Kitao, O.; Nakai, H.; Vreven, T.; Throssell, K.; Montgomery, J. A., Jr.; Peralta, J. E.; Ogliaro, F.; Bearpark, M. J.; Heyd, J. J.; Brothers, E. N.; Kudin, K. N.; Staroverov, V. N.; Keith, T. A.; Kobayashi, R.; Normand, J.; Raghavachari, K.; Rendell, A. P.; Burant, J. C.; Iyengar, S. S.; Tomasi, J.; Cossi, M.; Millam, J. M.; Klene, M.; Adamo, C.; Cammi, R.; Ochterski, J. W.; Martin, R. L.; Morokuma, K.; Farkas, O.; Foresman, J. B.; Fox, D. J. *Gaussian 16*, Revision A.03; Gaussian, Inc.: Wallingford CT, 2016.
(59) Hellweg, A.; Rappoport, D. Development of new auxiliary basis functions of the Karlsruhe segmented contracted basis sets including diffuse basis functions (def2-SVPD, def2-TZVPPD, and def2-QVPPD) for RI-MP2 and RI-CC calculations. *Phys. Chem. Chem. Phys.* **2015**, *17*, 1010−1017.
(60) Feller, D. The role of databases in support of computational chemistry calculations. *J. Comput. Chem.* **1996**, *17*, 1571−1586.
(61) Schuchardt, K. L.; Didier, B. T.; Elsethagen, T.; Sun, L.; Gurumoorthi, V.; Chase, J.; Li, J.; Windus, T. L. Basis Set Exchange: A Community Database for Computational Sciences. *J. Chem. Inf. Model.* **2007**, *47*, 1045−1052.
(62) Al-Kindy, S. M. Z.; Al-Sharji, N.; Al-Harasi, A. F.; Suliman, F. O.; Al-Lawati, H. J.; Schulman, S. Synthesis and spectroscopic study of 2,7-diethylamino-2-oxo-2H-chromen-3-yl benzothiazole-6-sulfonyl chlorides and its derivatives. *Arabian J. Chem.* **2017**, *10*, S114−S120.

DOI: 10.1021/acs.langmuir.9b01939
Langmuir 2019, 35, 12460−12468

(63) Kong, J.; Yu, S. Fourier Transform Infrared Spectroscopic Analysis of Protein Secondary Structures. *Acta Biochim. Biophys. Sin.* **2007**, *39*, 549−559.
(64) Tablet, C.; Matei, I.; Pincu, E.; Meltzer, V.; Hillebrand, M. Spectroscopic and thermodynamic studies of 7-diethylamino-coumarin-3-carboxylic acid in interaction with *β*- and 2-hydroxypropyl-*β*-cyclodextrins. *J. Mol. Liq.* **2012**, *168*, 47−53.
(65) Osuka, A.; Maruyama, K. Synthesis of Naphthalene-Bridged Porphyrin Dimers and Their Orientation-Dependent Exciton Coupling. *J. Am. Chem. Soc.* **1988**, *110*, 4454−4456.
(66) Liu, X.; Cole, J. M.; Chow, P. C. Y.; Zhang, L.; Tan, Y.; Zhao, T. Dye Aggregation and Complex Formation Effects in 7-(Diethylamino)-coumarin-3-carboxylic Acid. *J. Phys. Chem. C* **2014**, *118*, 13042−13051.
(67) Zhang, H.; Yu, T.; Zhao, Y.; Fan, D.; Chen, L.; Qiu, Y.; Qian, L.; Zhang, K.; Yang, C. Crystal structure and photoluminescence of 7-(N,N′-diethylamino)-coumarin-3-carboxylic acid. *Spectrochim. Acta, Part A* **2008**, *69*, 1136−1139.
(68) Kurouski, D.; Lu, X.; Popova, L.; Wan, W.; Shanmugasundaram, M.; Stubbs, G.; Dukor, R. K.; Lednev, I. K.; Nafie, L. A. Is supramolecular filament chirality the underlying cause of major morphology differences in amyloid fibrils? *J. Am. Chem. Soc.* **2014**, *136*, 2302−2312.
(69) Chou, K. C.; Nemethy, G.; Scheraga, H. A. Energetics of Interactions of Regular Structural Elements in Proteins. *Acc. Chem. Res.* **1990**, *23*, 134−141.
(70) Xing, Q.; Zhang, J.; Xie, Y.; Wang, Y.; Qi, W.; Rao, H.; Su, R.; He, Z. Aromatic Motifs Dictate Nanohelix Handedness of Tripeptides. *ACS Nano* **2018**, *12*, 12305−12314.
(71) Fu, Y.; Li, B.; Huang, Z.; Li, Y.; Yang, Y. Terminal Is Important for the Helicity of the Self-Assemblies of Dipeptides Derived from Alanine. *Langmuir* **2013**, *29*, 6013−6017.
(72) Wang, M.; Zhou, P.; Wang, J.; Zhao, Y.; Ma, H.; Lu, J. R.; Xu, H. Left or Right: How Does Amino Acid Chirality Affect the Handedness of Nanostructures Self-Assembled from Short Amphiphilic Peptides? *J. Am. Chem. Soc.* **2017**, *139*, 4185−4194.
(73) Lara, C.; Reynolds, N. P.; Berryman, J. T.; Xu, A.; Zhang, A.; Mezzenga, R. ILQINS hexapeptide, identified in lysozyme left-handed helical ribbons and nanotubes, forms right-handed helical ribbons and crystals. *J. Am. Chem. Soc.* **2014**, *136*, 4732−4739.
(74) Wang, J.; Liu, K.; Xing, R.; Yan, X. Peptide self-assembly: thermodynamics and kinetics. *Chem. Soc. Rev.* **2016**, *45*, 5589−5604.
(75) Koc, M. H.; Cinar Ciftci, G.; Baday, S.; Castelletto, V.; Hamley, I. W.; Guler, M. O. Hierarchical Self-Assembly of Histidine-Functionalized Peptide Amphiphiles into Supramolecular Chiral Nanostructures. *Langmuir* **2017**, *33*, 7947−7956.
(76) Lu, K.; Jacob, J.; Thiyagarajan, P.; Conticello, V. P.; Lynn, D. G. Exploiting Amyloid Fibril Lamination for Nanotube Self-Assembly. *J. Am. Chem. Soc.* **2003**, *125*, 6391−6393.

DOI: 10.1021/acs.langmuir.9b01939
Langmuir 2019, 35, 12460−12468